PCCP

ROYAL SOCIETY OF CHEMISTRY

PAPER

View Article Online
View Journal | View Issue

Cite this: *Phys. Chem. Chem. Phys.*, 2021, **23**, 12051

Ultrafast geometrical reorganization of a methane cation upon sudden ionization: an isotope effect on electronic non-equilibrium quantum dynamics†

Cayo E. M. Gonçalves,[a] R. D. Levine[b] and F. Remacle *[ab]

Received 8th March 2021,
Accepted 29th April 2021

DOI: 10.1039/d1cp01029h

rsc.li/pccp

The ultrafast structural, Jahn–Teller (JT) driven, electronic coherence mediated quantum dynamics in the CH_4^+ and CD_4^+ cations that follows sudden ionization using an XUV attopulse exhibits a strong isotope effect. The JT effect makes the methane cation unstable in the T_d geometry of the neutral molecule. Upon the sudden ionization the cation is produced in a coherent superposition of three electronic states that are strongly coupled and neither is in equilibrium with the nuclei. In the ground state of the cation the few femtosecond structural rearrangement leads first to a geometrically less distorted D_{2d} minimum followed by a geometrical reorganization to a shallow C_{2v} minimum. The dynamics is computed for an ensemble of 8000 ions randomly oriented with respect to the polarization of the XUV pulse. The ratio, about 3, of the CD_4^+ to CH_4^+ autocorrelation functions, is in agreement with experimental measurements of high harmonic spectra. The high value of the ratio is attributed to the faster electronic coherence dynamics in CH_4^+.

1. Introduction

The ground state (GS) of the methane cation is unstable in the T_d geometry that corresponds to the equilibrium geometry of the neutral molecule. Sudden ionization of the neutral methane molecule produces a methane cation in the T_d geometry that corresponds to the equilibrium geometry of the neutral molecule. The Jahn–Teller (JT) effect causes an immediate structural rearrangement of the nascent cation. The sudden ionization leads to a superposition of the three electronic states that are degenerate in the T_d geometry. An ultrafast, few femtosecond (fs), non-adiabatic dynamics triggered by the JT effect therefore sets on right after the ionization when the non-equilibrium electronic density resulting from the initial coherent superposition of electronic states is still localized in the Franck–Condon region. We investigate how the spatio-temporal localizations of the non-adiabatic amplitude transfers are mediated by the ultrafast electronic coherences resulting from the sudden ionization. This ultrafast coupled electronic–nuclear dynamics makes the structural nuclear rearrangement a test case for the role of electronic coherences in attochemistry.[1–9]

The first 2–3 fs of the rearrangement of the methane cation has been experimentally probed by high harmonic generation (HHG) spectroscopy.[10,11] A strong isotopic effect on the CD_4/CH_4 harmonic spectra has been reported, with CD_4 leading to a higher yield in emitted harmonics than CH_4 by about a factor of 3 after 1.6 fs.[10,11] The proposed explanation was that because of the slower motion of the nuclei, the time autocorrelation function, $|C(t)|^2$, of the initial state, $|\Psi(0)\rangle$, defined as $|C(t)|^2 = |\langle\Psi(0)|\Psi(t)\rangle|^2$, falls more slowly for CD_4^+ than for CH_4^+ at the time when the electron recollides with the cation.[12] In addition, the isotope effect in CD_4/CH_4 was found to be larger than that in D_2/H_2, which is not simply consistent with the changes in reduced mass.

We report here a computational study on the early, few fs, time structural quantum dynamics in CH_4^+ and CD_4^+ upon sudden ionization using an XUV attopulse. Our aim is to determine the sequence of primary changes and whether the electronic coherences resulting from the sudden ionization play a role in the large ratio of the autocorrelation functions of CD_4^+ and CH_4^+. The Franck–Condon (FC) region is centered on the T_d geometry of the ground state of the neutral molecule, a geometry that is unstable in the cation. The equilibrium geometry of the cation ground state corresponds to a very shallow C_{2v} minimum that is quasi-degenerate with a D_{2d} minimum.[13–16] Is the less distorted D_{2d} configuration

[a] *Theoretical Physical Chemistry, University of Liège, 4000 Liège, Belgium. E-mail: fremacle@uliege.be*
[b] *The Fritz Haber Research Center for Molecular Dynamics, The Hebrew University of Jerusalem, 91904 Jerusalem, Israel*

† Electronic supplementary information (ESI) available: Computational methods, and supplementary figures and tables. See DOI: 10.1039/d1cp01029h

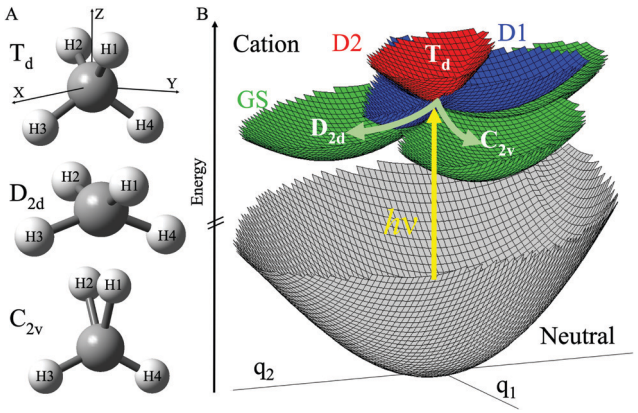

Fig. 1 (A) Geometries of the GS of the cation: T_d geometry and the orientation of the body frame, and D_{2d} and C_{2v} equilibrium geometries. (B) A 3D plot of the 2-dimensional PES of the three lowest electronic states of the cation: Green, GS; blue, first excited state, D1; red, second excited state, D2, together with the GS of the neutral molecule (grey). The plot is *vs.* two reduced coordinates: q_1, pointing to the C_{2v} minimum; and q_2, pointing to the D_{2d} minimum of the GS cation.

populated before the C_{2v} minimum in the very early time dynamics? This is physically reasonable since only the HCH angles need to be significantly modified during the T_d to D_{2d} rearrangement which requires a smaller structural distortion. What is the role of the non-equilibrium dynamics and of the JT non-adiabatic coupling (NAC) in the large isotope effect on the high harmonic yields as measured experimentally?[10,11] Is there indeed clear evidence for a role of non-equilibrium electronic density in the very early times?

In the passage to the D_{2d} geometry the four C–H bond lengths essentially remain equal and only the valence HCH angles change with respect to the T_d geometry of the neutral molecule, while in the C_{2v} geometry, both angles and bond lengths are substantially modified, see Fig. 1A. The C_{2v} and D_{2d} geometries are in the vicinity of the FC region that is defined by the ground vibrational state of the neutral molecule in its equilibrium geometry, as shown in Fig. 1B.

Patchkovskii[17] related the large isotope effect observed in the high harmonic yields of the methane cation compared to that of D_2/H_2 and its effect on the decay of the autocorrelation function, $|C(t)|^2$, to the steepness and the change in curvature of the potential energy surfaces (PES) around the JT unstable geometry. The structural rearrangement of early time JT dynamics in CH_4^+ and CD_4^+ has been studied using a quasivibronic coupling scheme[18] for the 3 lowest excited states by Mondal and Varandas up to full 9 nuclear dimensions[14–16] within the Condon approximation, assuming photoionization matrix elements independent of the nuclear geometry and neglecting the dependence of the ionization yields on the orientation of the electric field. These computations allow identifying the key role of the e and t_2 vibrational normal modes of the T_d geometry in the distortion leading to the C_{2v} minimum as well as the role of the t_2 mode in the distortion leading to the D_{2d} minimum. They confirm the ultrafast time scale of the isotope effect experimentally observed[10,11] and point to the fact that it is important to at least include the e and t_2 normal modes to realistically describe the short time dynamics up to 1.6 fs.[14] The HHG spectra reported by Madsen *et al.*[19] also confirm the involvement of the same modes. Section 2 discusses the new features in our numerically accurate quantum dynamical computation.

2. Results and discussion

Our quantum dynamical results reveal that in the cation ground state (GS) the D_{2d} basin is populated before the C_{2v} one. The strong isotopic effect in the early 1–2 fs dynamics is found to be related to electronic coherences and ensuing amplitude transfers from the 1st (D1) and 2nd (D2) excited states to the GS (D0) of the cation. These results are robust against averaging the quantum dynamics over an ensemble of 8000 initial states that span the FC region in the three lowest excited states determined from the sudden ionization of molecules randomly oriented with respect to the polarization of the XUV pulse.

2.1 Multi-state ensemble quantum dynamics on a 2D grid

To investigate the dynamics, we solve the time-dependent Schrödinger equation on a 2-dimensional nuclear coordinate system for the three lowest states of the methane cation that are non-adiabatically coupled due to the JT effects (see Computational methods in the ESI† for more details). The two coordinates, q_1 and q_2, are defined as a linear combination of Cartesian displacements (see Table S1, ESI†) that lead to the specific C_{2v} (q_1) and D_{2d} (q_2) minima shown in Fig. 1B and include small distortions in order to span the NAC seams.

The q_1 coordinate has significant amplitudes on the components of the two t_2 and e modes involved in the JT distortion and the q_2 coordinate has components of the e mode (see Table S2 of the ESI†). In addition, both coordinates have small amplitudes in the a_1 mode. Outside of the T_d geometry in the FC region, q_1 and q_2 have amplitudes in the normal modes of the C_{2v} and D_{2d} forms involved in the NAC seams, see Tables S3 and S4 of the ESI.† The coordinates q_1 and q_2 therefore capture the motions along the e and t_2 normal modes of T_d identified in ref. 14 to be crucial for describing the short time dynamics.

The electronic structure at each grid point is computed at the SA-CASSCF (9,8)/6-31G++(2df,2pd) level for the three lowest states of the cation and CASSCF (10,8)/6-31G++(2df,2pd) for the GS of the neutral using MOLPRO.[20] The computed vertical ionization energy to the T_d point is 13.61 eV. In the cation GS, the C_{2v} minima correspond to the lowest energy, and the D_{2d} minimum is 0.2837 eV above in agreement with ref. 13, see Tables S5–S7 (ESI†) for the equilibrium geometries. The three potential energy surfaces (PES) on the 2D grid are shown in Fig. 1B (see also Fig. S1 for isocontour plots in the ESI†). The three PES have very different steepnesses around the T_d geometry. The gradient around the T_d geometry is steeper for the GS than for the D1 state, while the minimum of the D2 state coincides with the T_d geometry and the D2 PES is very steep

around the minimum. The minima corresponding to C_{2v} and D_{2d} in the GS occur in a very shallow region of the potential, while the D1 minima are localized close to the NAC seams. In the GS, in addition to the two wells that correspond to slightly distorted D_{2d} and C_{2v} geometries at (−1.4,0) and (0,−1.12), respectively, there is also a third minimum close to a C_s symmetry at (1.08,1.26). We describe the geometry on a grid using 146 grid points for q_1 and 184 for q_2, which leads to 26 864 grid points per electronic state. See the ESI† for more details. Our aim here is to provide a realistic description of the initial state of the cation resulting from a sudden ionization process induced by XUV pulses with different energies, taking into account the orientation of the molecule with respect to the polarization direction of the ionizing pulse, see Sections 2.2 and 2.3. Since it is not possible with present computational resources to define the initial states and solve the time-dependent Schrödinger on a grid for the full dimensionality of the nuclear motion, we define the two coordinates q_1 and q_2 that allows capturing the essential features of the nuclear dynamics in the first dozen of fs of the dynamics.

2.2 Sudden photoionization and initial state non-equilibrated electronic density

The definition of a realistic initial state is a crucial point in determining the short time dynamics resulting from the sudden photoionization of the GS of the neutral molecule. We use a sudden approximation which is justified by the short, sub-fs, duration of the pulse and the fact that XUV attopulses are weak so that only one photon absorption can occur. For such weak, attosecond, few cycle pulses, it is therefore a good approximation to consider that the maximum of the ionization occurs at the maximum of the electric field and to neglect the electronic and nuclear dynamics during the pulse. An extreme level of the sudden approximation is to assume that the sudden ionization process creates a hole in one of the molecular orbitals of the neutral molecule. It has been used in early studies of charge migration.[6,21–23] Here we compute explicitly all the photoionization amplitudes that define the coherent superposition of the electronic states[24–26] for each grid point in the Franck–Condon region. We therefore take into account the strong variation of the photoionization cross sections to the three electronic states of the cation as a function of the geometry in the FC region of the neutral ground state. In addition, typically, experiments are done for randomly oriented molecules with respect to the polarization of the ionizing pulse. We therefore average the quantum dynamics over an ensemble of orientations with respect to the electric field.

At each point, g, of the 2D grid, the amplitudes of the initial states in the three electronic states of the randomly oriented CH_4^+/CD_4^+ ions, c_{ig}^m, are defined as the photoionization amplitude to electronic state i weighted by the neutral vibrational ground state $c_{GS,g}^{neut}$: $c_{ig}^m = c_{GS,g}^{neut}\sqrt{\rho(\varepsilon)}\,\hat{\mathbf{e}}.\mathbf{d}_{ig}^{\varepsilon}$, see the ESI† for the details. In c_{ig}^m, m represents a given orientation, $\hat{\mathbf{e}}_m = \mathbf{E}_m/|E|$, of the electric field of the ionizing pulse with respect to the laboratory frame shown in Fig. 1A and ig is the index notation for electronic state i and grid point g. $\mathbf{d}_{ig}^{\varepsilon}$ is the transition dipole from the GS of the neutral to the continuum of the ith electronic state at grid point g integrated over the solid angle $\hat{\Omega}$, with ε being the kinetic energy of the photoelectron computed at grid point ig. $\rho(\varepsilon)$ is the density of photoelectron states.

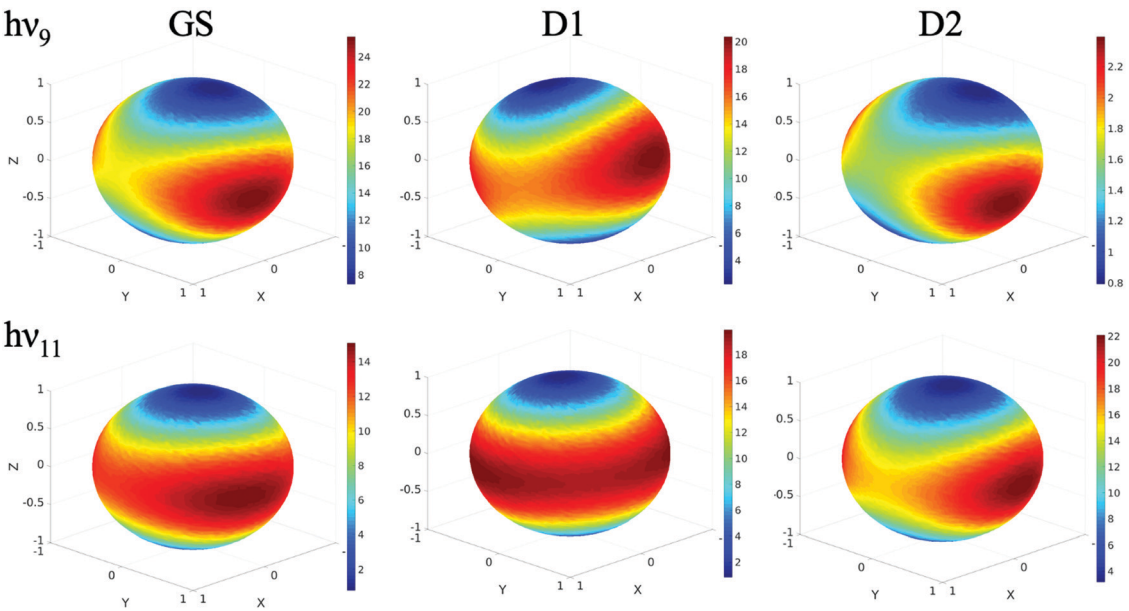

Fig. 2 Heatmaps of the angularly resolved photoionization yields plotted separately for each electronic state ($\sum_g \left|c_{ig}^m\right|^2$ with i = GS, D1 and D2) computed for CH_4^+ and two carrier frequencies of the ionization XUV attopulse ($h\nu_9$ = 13.95 eV and $h\nu_{11}$ = 17.05 eV). The heatmaps are computed by drawing 8000 random orientations, $\hat{\mathbf{e}}_m$, of the electric field. (X,Y,Z) represent the Cartesian coordinates of the unit vector $\hat{\mathbf{e}}_m = \mathbf{E}_m/|\mathbf{E}|$ with respect to the body frame shown in Fig. 1A. Note how for the D2 state the yield is very small for the 9th harmonic, while it is comparable to the lowest states for the 11th one. See Fig. S2 of the ESI† for the photoionization yields of CD_4^+.

The norms of the initial states, $|\mathbf{c}_m|^2 = \sum_{ig} \left|c_{ig}^m\right|^2$, are proportional to the total angularly resolved photoionization yields. The computed photoionization angular maps are plotted for CH_4^+ in Fig. 2 separately for each electronic state. The plot is a heatmap on the unit sphere.

In order to investigate the role of the multistate dynamics in the isotope effect, we selected two carrier frequencies of the ionizing XUV attopulses: 13.95 and 17.05 eV. These frequencies correspond to the 9th and 11th harmonics of the XUV attopulses that can be produced by HHG with 800 nm laser pulses: $h\nu_9$ = 13.95 and $h\nu_{11}$ = 17.05 eV respectively. Photoionization using the $h\nu_9$ pulse builds a non-stationary wave packet on the cation with 54% population in the GS, 41% in the D1 state and a small amount of population in D2 (5%). On the other hand, all three states of the cation are accessed using the $h\nu_{11}$ pulse, which leads to 26% of the population in the GS, 37% in D1 and 37% in D2. Overall, the total ionization yield for the $h\nu_{11}$ pulse is 14% higher than that for the $h\nu_9$ one. There is no significant difference in the main features of the angularly resolved yields computed for CD_4^+ shown in Fig. S2 of the ESI,† since the energetics of the electronic states are the same for the two ions and the total yields in the three electronic states are in the same ratios. However, the isotope substitution affects the spreading of the ground vibrational state of the neutral molecule which is narrower in the case of CD_4^+. This leads to a smaller extension of the FC region for CD_4^+. As we discuss below, this isotope effect has important consequences for the localization of the initial states and the subsequent multistate dynamics.

The vectors, $\mathbf{c}_m$, of the initial states on the grid define an ensemble with a density matrix $\rho_{\text{ens}}(0)$, $\rho_{\text{ens}}(0) = \sum_m^M \rho_m(0) = \sum_m^M \mathbf{c}_m \mathbf{c}_m^\dagger$, which is the sum of the M pure case density matrices, $\rho_m(0)$. M is the number of orientations of the electric field of the ionizing pulse with respect to the laboratory frame shown in Fig. 1A. M needs to be quite large in order to get an accurate sampling of the orientations. We use M = 8000 for computing the heatmaps shown in Fig. 2. We demonstrate in the Computational methods of the ESI† that the ensemble density matrix $\rho_{\text{ens}}(0)$ is very rank deficient and possesses only three non-zero eigenvalues. Its spectral representation then takes the form: $\rho_{\text{ens}}(0) = \sum_{r=1}^{3} \omega_r{}^2 \mathbf{s}_r \mathbf{s}_r^\dagger$. This feature leads to a considerable saving of computer time for getting an accurate ensemble averaging of the quantum dynamics over orientations. The time evolution of each component, $\rho_m(0)$, of the ensemble density matrix is unitary and therefore the ensemble density matrix, $\rho_{\text{ens}}(0)$, will also evolve under a unitary transformation. To describe the ensemble dynamics, it is therefore numerically strictly equivalent to solve the time-dependent Schrödinger equation on the grid for the three eigenvectors $\mathbf{s}_r$, r = 1, 2, 3, of the ensemble density matrix that correspond to non-zero eigenvalues or to solve it for the 8000 $\mathbf{c}_m$ vectors. More details can be found in Computational methods of the ESI.†

We show in Fig. 3 the initial localization in the Franck–Condon region of the diagonal elements of $\rho_{\text{ens}}(0)$, $[\rho_{\text{ens}}(0)]_{ig,ig} = \sum_m \left|c_{ig}^m\right|^2$ on the 2D grid points g separately for the three electronic states, i = GS, D1 and D2, computed for CH_4^+ for the two wavelengths of the ionizing pulse, $h\nu_9$ in the top row and $h\nu_{11}$ in the bottom one. The localization patterns of the initial state in each electronic state exhibit the same features for the two pulses, but the initial states obtained for the $h\nu_{11}$ pulse are more spread. The localization of

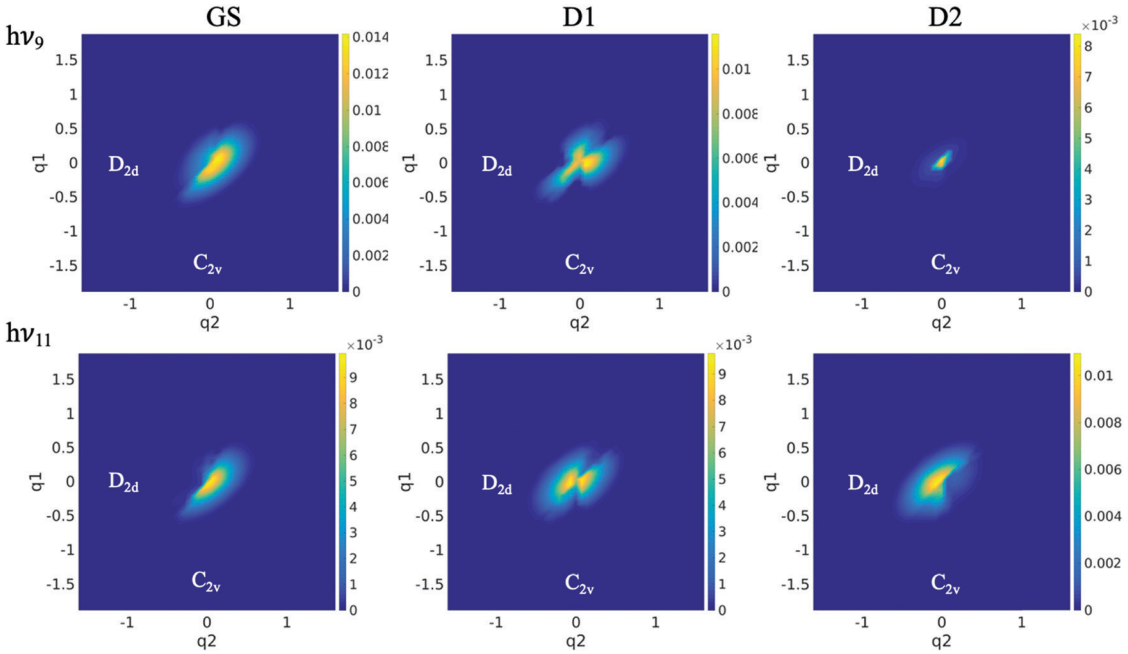

Fig. 3 Heatmaps of the initial population at each grid point, $[\rho_{\text{ens}}(0)]_{ig,ig}$ in each electronic state i = GS (left), D1 (middle) and D2 (right), computed for CH_4^+ for the $h\nu_9$ (top row) and $h\nu_{11}$ (bottom row) pulses. See Fig. S3 (ESI†) for CD_4^+.

the initial state is asymmetrically distributed along the $q_1 = q_2$ diagonal for the GS and the D2 state. The initial localization in the GS (left column in Fig. 3) has a larger extension in the lower diagonal part, towards the C_{2v} region at (−1.4,0) (q_1,q_2) coordinates, while for the D2 state (right column), the initial state has a larger extension in the upper diagonal part, towards the D_{2d} minimum at (0,−1.12). The localization in the D1 state tends to be more evenly distributed between the two regions. The same patterns are observed for CD_4^+ shown in Fig. S3 (ESI†), but overall the initial density is more localized around the T_d region because the CD_4 neutral vibrational ground state is less spread around the T_d geometry due to the mass effect.

2.3 Dynamics of the ultrafast Jahn–Teller nuclear rearrangement to D_{2d} and C_{2v}

The time evolution of the total population in each electronic state averaged over the ensemble is shown in Fig. 4A and B for ionization with the $h\nu_9$ and $h\nu_{11}$ pulses, respectively, in full lines for CH_4^+ and in dashed lines for CD_4^+. The GS and the D1 state are about equally accessed using the $h\nu_9$ pulse with only a small fraction (5%) in the D2 state. The population transfers between the three states are rather monotonic with very little differences between the two isotopes, and a smooth decay from the D1 state to the GS, while the D2 state remains mostly decoupled from the two lowest ones during the first 24 fs dynamics. On the other hand, for the $h\nu_{11}$ pulse, the three electronic states are about equally accessed by the sudden ionization process. There is a rich non-adiabatic dynamics between the three states at early times, with large amplitude oscillations of the populations in the D1 and D2 states and a more monotonic increase of the population in the GS. The wave packets are moving over the grid with rates determined by the gradients of the potentials, which, as can be seen from Fig. 1B and Fig. S1 (ESI†), are very different: The minima in the GS are very shallow. The gradients are larger in D1 and D2. The wells in D1 are deeper and located in the close vicinity of the NAC seams. D2 has a single deep well in the T_d region where the non-adiabatic couplings are the largest, see Fig. S4 (ESI†). These topologies of the D1 and D2 PES favor efficient population transfer from the two higher states to the GS. The oscillations of the populations do not occur with a definite period because of vibrational coherences on each potential energy surface and of the complex dynamics of the electronic coherences between the three states shown in Fig. S5 (ESI†). The periods of the electronic coherences are given by the energy difference between the two states involved and vary with the localization of the wave packets on the grid. Their amplitudes are modified by the transfers between the states in the NAC region couplings. Heatmaps of the NAC matrix elements on the grid, $\tau_{ij}(g)$, are shown in Fig. S4 (ESI†). One can see that NAC seams form a dense network of regions of efficient amplitude transfer. Overall the periods of the oscillations in the

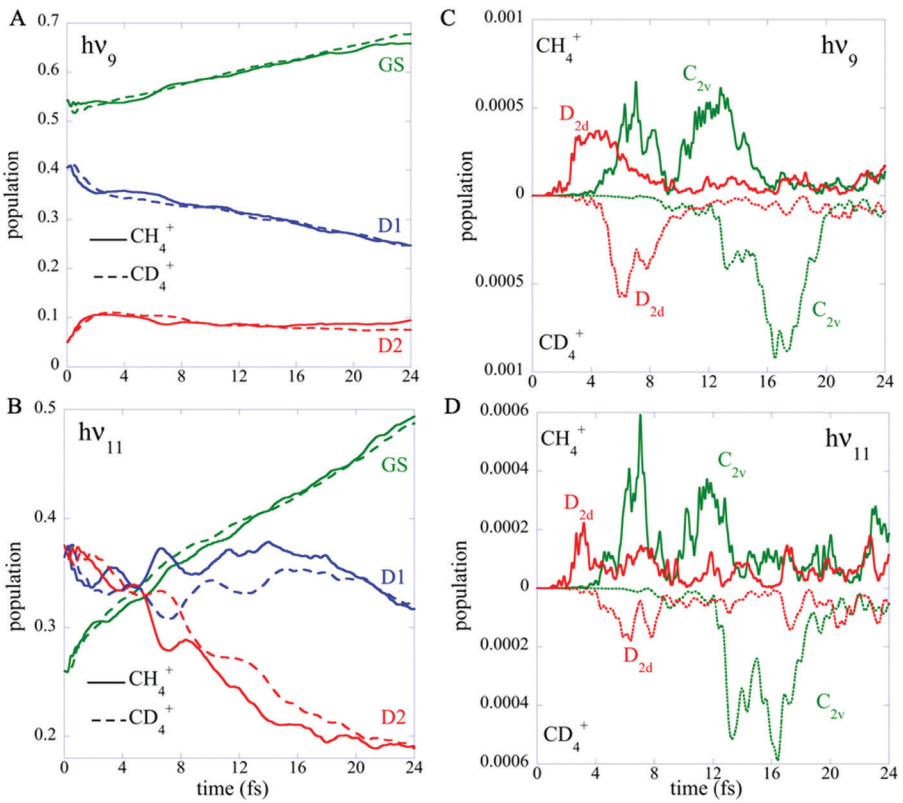

Fig. 4 (A and B) Early time population dynamics of CH_4^+ (full lines) and CD_4^+ (dashed lines) computed for sudden ionization with the $h\nu_9$ pulse (panel A) and the $h\nu_{11}$ pulse (panel B) in the three electronic states of the cation (GS: green, D1: blue and D2: red). (C and D) Populations of the grid point corresponding to the D_{2d} (red) and C_{2v} (green) minima of the GS computed for CH_4^+ and CD_4^+ with the $h\nu_9$ pulse (panel C) and the $h\nu_{11}$ pulse (panel D).

populations plotted in Fig. 4B for the $h\nu_{11}$ pulse are about 3 fs in CH_4^+ (full lines) and longer in CD_4^+ (dashed lines), for which they are between 4 and 6 fs. After $\approx$15 fs, the non-adiabatic transfers are more monotonic and the isotopic effect is less pronounced. When a wave packet involving several electronic states reaches a NAC region, one can show algebraically that the population transfers are governed by the electronic coherences.[27] Such a strong isotopic effect on the population transfers due to NAC driven by electronic coherences has already been reported for N_2[28–30] and LiH.[31]

The time scale and the efficiency of the transfers to the D_{2d} and C_{2v} regions of the GS on the grid result from the interplay between the localization of the initial states resulting from the sudden ionization shown in Fig. 2, the motion of the wave-packets in the ground state of the cation and the network of NAC seams shown in Fig. S4 (ESI†) that allow transfer from the D1 and D2 states. As we show in Fig. 2, the localization of the initial state in the GS is skewed towards the D_{2d} region, while it is more evenly spread in the D1 electronic state and skewed to the C_{2v} region in D2. On the other hand, the localization of the network of NAC seams (Fig. S4, ESI†) does not favor one minimum or the other.

The populations of the grid points that correspond to the C_{2v} and D_{2d} minima of the GS are plotted in Fig. 4C and D for ionization with the $h\nu_9$ and $h\nu_{11}$ pulses respectively. One clearly sees that the D_{2d} minimum (red) is visited first by the wave packet with a maximum at 4 fs for CH_4^+ and 7 fs for CD_4^+. This occurs before the increase in the C_{2v} minimum grid point and the concomitant decay in the D_{2d} one. One does not observe a significant difference in the increase of population in the D_{2d} minimum for ionization by the $h\nu_9$ or $h\nu_{11}$ pulses, which suggests that the early population of the D_{2d} minimum results from the GS dynamics. This is supported by the fact that, comparatively, the maximum of population in the D_{2d} minimum is about half for the $h\nu_{11}$ pulse (Fig. 4D) than for the $h\nu_9$ pulse in agreement with the smaller population in the GS for an ionization with the $h\nu_{11}$ pulse. The respective increases in the D_{2d} and C_{2v} minima are delayed for CD_4^+ at $\approx$5 fs and $\approx$12–13 fs compared to $\approx$1.5 fs and 5 fs for CH_4^+. We show in Fig. S6 (ESI†) the populations computed in larger regions (25 points) around the two minima which represent $\approx$5 to

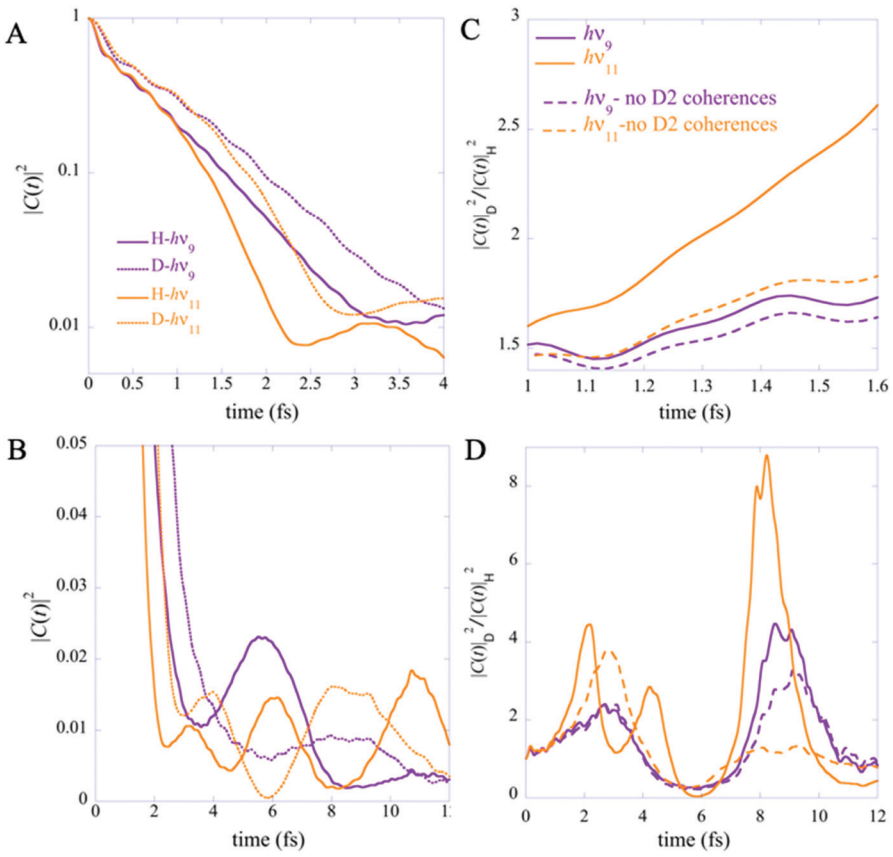

Fig. 5 (A) The square modulus of autocorrelation function, $|C(t)|^2$, on a log-linear scale, computed for the $h\nu_9$ pulse in violet and for the $h\nu_{11}$ pulse in orange, CH_4^+ in full lines and CD_4^+ in dotted lines. (B) Long time small recurrences of $|C(t)|^2$ on a linear scale. (C) The $|C(t)|_D^2/|C(t)|_H^2$ ratios for the $h\nu_9$ (violet) and the $h\nu_{11}$ pulse (orange) at short times, computed including the GS–D2 and D1–D2 coherence terms (full lines) and without them (dashed lines). (D) The $|C(t)|_D^2/|C(t)|_H^2$ ratios at longer times.

10% of the population in the GS. For these larger regions, the population in the D_{2d} region clearly increases before that in the C_{2v} region too. For completeness, in Fig. S6 (ESI†), we also added the population in a region of 25 grid points in the C_s minimum. One can see that the onset of the increase of population in this minimum is intermediate between those of the D_{2d} and C_{2v} regions.

2.4 Electronic coherence mediated isotope effect

The square moduli of the autocorrelation functions of the initial states, $|C(t)|_H^2$ and $|C(t)|_D^2$, are plotted in Fig. 5A on a log-linear scale. As expected, because of the mass difference, the initial decay of $|C(t)|_D^2$ is slower than that of $|C(t)|_H^2$ and the decay rates out of the initial state are very similar for the two pulses up to 1.5 fs. After 3 fs, the initial decay is over and the overlap of the wave packet with its initial location is very small. The small amplitude recurrences of $|C(t)|_H^2$ and $|C(t)|_D^2$ at longer times are shown in Fig. 5B. As shown explicitly by eqn (1), the autocorrelation function of the initial state is an observable that is sensitive to the electronic coherences:

$$|C(t)|^2 = \sum_{i=1}^{3}\sum_{gg'} c_{ig}(0)c_{ig}(t)c_{ig'}(0)c^*_{ig'}(t) + \sum_{i,j\neq i}^{3}\sum_{gg'} c_{ig}(0)c_{ig}(t)c_{jg'}(0)c^*_{ig'}(t) \quad (1)$$

where i, j = GS, D1 and D2. The $|C(t)|_D^2/|C(t)|_H^2$ ratio is plotted in Fig. 5C for short times, from 1 to 1.6 fs, for the two ionizing pulses, $h\nu_9$ in violet and $h\nu_{11}$ in orange, with (full lines) and without (dashed lines) including the coherence terms that involve the D2 state (GS–D2 and D1–D2) in eqn (1). The longer time behavior of the ratio is shown in Fig. 5D.

One can see from Fig. 5C and D that the value of $|C(t)|_D^2/|C(t)|_H^2$ oscillates and $|C(t)|_D^2/|C(t)|_H^2$ can reach large values, much larger than the $\approx$1.5 ratio that is expected from the mass effect. Such large values are also reported in ref. 14.

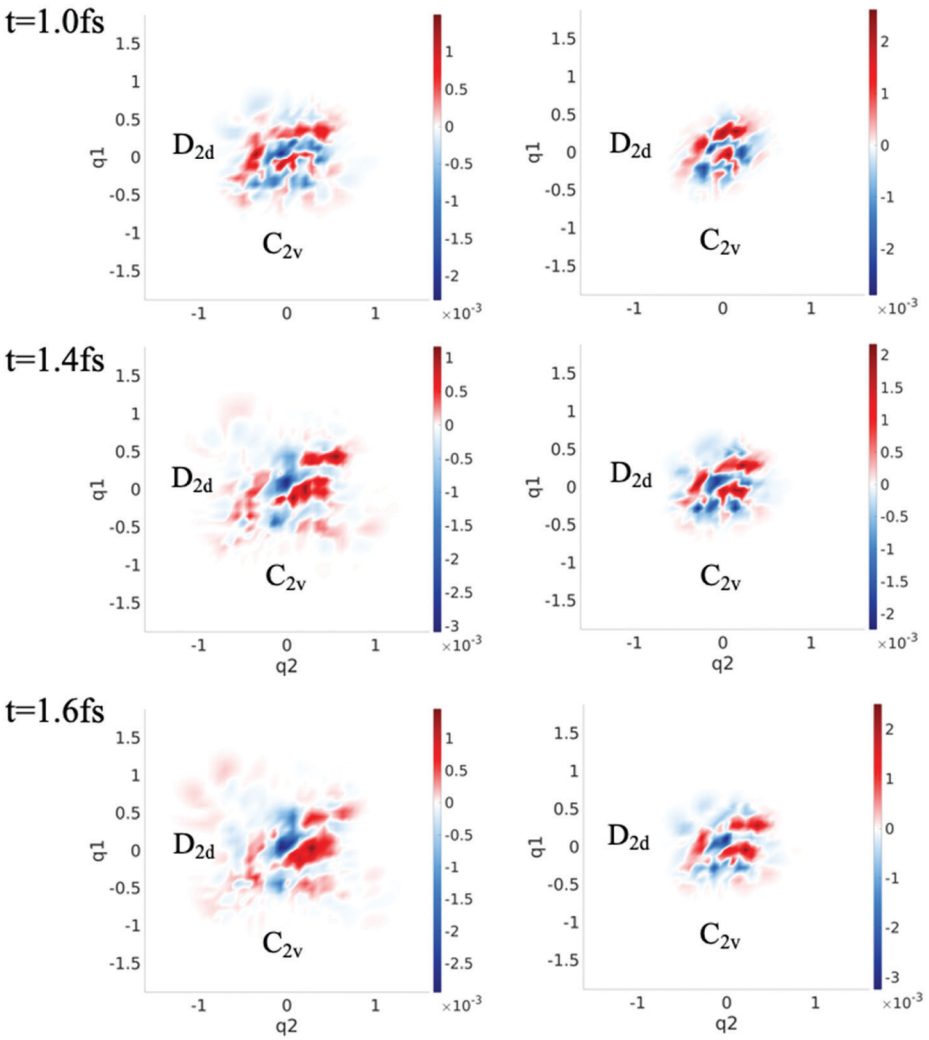

Fig. 6 Snapshots of the localization of the real part of the GS–D2 electronic coherence (left CH_4^+, right CD_4^+) computed for the $h\nu_{11}$ pulse. Top row: t = 1 fs, middle row: t = 1.4 fs, bottom row: t = 1.6 fs. Note how the GS–D2 coherence delocalizes towards D_{2d} for CH_4^+, while it has not migrated yet out of the FC region for CD_4^+.

The oscillating patterns in Fig. 5D are governed by the oscillations of the electronic coherences (see also Fig. S5 and S6, ESI†). The faster increase of the computed $|C(t)|_D^2/|C(t)|_H^2$ ratio for the $h\nu_{11}$ initial state in the range 1 to 2 fs and its larger amplitude oscillations at 2, 4.5 and 8 fs (Fig. 5D) can be traced to the large amplitude of the GS–D1, GS–D2 and D1–D2 electronic coherences shown in Fig. S5 (ESI†), which are delayed for CD_4^+ compared to CH_4^+. More specifically, the comparison between the computed value of the ratio including and not including the D2 coherent terms in eqn (1) in Fig. 5C and D shows that the $|C(t)|_D^2/|C(t)|_H^2$ ratio is strongly influenced by the electronic coherences that involve the D2 state. The longer period of the GS–D2 coherence in CD_4^+ leads to maxima at 2 and 4.5 fs in the $|C(t)|_D^2/|C(t)|_H^2$ ratio (Fig. 5D), while there is only one broad peak with a maximum at 3 fs for the ionization using the $h\nu_9$ pulse.

Fig. 5C shows the behavior of the $|C(t)|_D^2/|C(t)|_H^2$ ratio in the time range for which the experimental harmonic yield ratio was reported in ref. 10. For the $h\nu_{11}$ pulse, the computed ratio (orange) is in excellent agreement with the ratio of the yields in high harmonics reported in ref. 10. It is equal to 1.7 at 1 fs compared to an experimental value of the ratio of harmonic yields of 1.75, and at 1.6 fs, the computed ratio is 2.6 compared to a value of 3 for the ratio of the harmonic yields. The agreement is less good for ionization with the $h\nu_9$ pulse, with a computed value of $\approx$1.5 for the entire range [1,1.6] fs. This suggests that the very early time non-equilibrium electronic dynamics involving the three electronic states of the cation plays a crucial role in leading to a large isotope effect at short times and strongly depends on the initial state created by the ionization process. While the initial state of the cation in ref. 10 results from tunneling ionization, we here report results for an initial state resulting from a photoionization process which allows controlling the initial population in each electronic state by varying the photon energy. Since for the ionization using the $h\nu_{11}$ pulse, there are similar amounts of population in the three states, the fast oscillations of the GS–D2 coherence have a large amplitude, while the amplitude of the GS–D2 coherence is very small for the $h\nu_9$ pulse for which the population in the D2 state is very small. The first oscillation of the GS–D2 coherence decays faster for CH_4^+ than for CD_4^+ in the first 2 fs of the dynamics of the decay of the autocorrelation functions of the two isotopes which leads to the higher ratio, $|C(t)|_D^2/|C(t)|_H^2$, of the initial state created with the $h\nu_{11}$ pulse. Snapshots of the localization of the real part of the GS–D2 electronic coherence, $\rho_{02,g}(t)$, on the grid are plotted in Fig. 6 for CH_4^+ and CD_4^+ for ionization with the $h\nu_{11}$ pulse. One clearly sees the faster delocalization of the GS–D2 electronic coherence to the D_{2d} region by $\approx$1.6 fs for CH_4^+, while it has hardly moved out of the FC region for CD_4^+. The GS–D1 and D1–D2 electronic coherences also visit the D_{2d} region at very short times, before 4 fs.

3. Conclusions

Sudden photoionization produces a methane cation in the equilibrium geometry of the neutral molecule as a coherent superposition of three distinct electronic states. These adiabatic states are coupled by a Jahn–Teller distortion. Quantum mechanical dynamical computations on accurate potential energy surfaces and couplings show that electronic coherences play a key role in the early time evolution of the coupled electronic–nuclear states. In particular, the rate of population transfer is governed by the coherence terms,[27] which leads to an isotope effect on the dynamics between the electronic states larger than the one expected on the basis of the mass ratio. We already reported such a strong effect for the isotopomers of the diatomic molecules N_2[28–30] and LiH.[31] This results in a significant isotopic difference between CH_4^+ and CD_4^+, which is robust when averaged over random orientations of the molecule with respect to the polarization of the photoionizing pulse. The magnitude of the effect on the ratio of the autocorrelations for a photon energy of the ionizing pulse that significantly populates the D2 state is comparable to that reported experimentally using high harmonic generation spectroscopy[10] for a tunneling ionization process. The dynamics are computed by averaging over an ensemble of 8000 different initial conditions corresponding to the orientation of the neutral molecule with respect to the laser pulse. There are, however, just three principal components to that ensemble and propagating them allows for a computationally efficient implementation.

The strong isotope effect in the early 1–2 fs dynamics is shown to be related to electronic coherences whose spatial and temporal localizations govern the amplitude transfers from the D1 and D2 excited states of the cation to specific regions of the GS cation potential. In the ground state the shallow basin around the less distorted D_{2d} geometry is accessed first and is followed by a rearrangement into the C_{2v} geometry where both the bonds and the angles are modified. The D_{2d} geometry is established by about 4 fs for CH_4^+ and at 8 fs for CD_4^+. Primarily this is due to the variations of the photoionization matrix elements with the geometry of the ground state in the Franck–Condon region that lead to different localizations of the initial state resulting from the sudden photoionization process. Such ultrafast electronic and structural rearrangements in cations ionized to multiple interfering channels are ideally probed by HHG spectroscopy,[1,32,33] which provides the needed sub- to few-fs time resolution. Recent developments in 3D two electron angular streaking[34] and time-resolved X-ray transient absorption spectroscopy[5,35–38] could also shed light on such ultrafast processes.

Conflicts of interest

There are no conflicts to declare.

Acknowledgements

This work was supported by the Fonds National de la Recherche Scientifique (Belgium), F.R.S.-FNRS research grants #T.0132.16 and #J.0012.18 and the AMOS program within the Chemical Sciences, Geosciences and Biosciences Division of the Office of

Basic Energy Sciences, Office of Science, US Department of Energy, Award #DE-SC0012628. Computational resources were provided by the Consortium des Equipements de Calcul Intensif (CECI), funded by the F. R. S.-FNRS under Grant #2.5020.11. Support of the COST action Attochem (CA18222) is also acknowledged. We thank Prof. Wen Li for useful discussions on the experimental aspects, Dr Stephan van den Wildenberg for the computation of the photoionization matrix elements and Dr Benoit Mignolet for his careful reading of the manuscript.

References

1 M. Nisoli, P. Decleva, F. Calegari, A. Palacios and F. Martín, *Chem. Rev.*, 2017, **117**, 10760–10825.
2 *Attosecond molecular dynamics*, ed. M. J. J. Vrakking and F. Lepine, The Royal Society of Chemistry, Cambridge, 2019.
3 A. Marciniak, V. Despré, V. Loriot, G. Karras, M. Hervé, L. Quintard, F. Catoire, C. Joblin, E. Constant, A. I. Kuleff and F. Lépine, *Nat. Commun.*, 2019, **10**, 337.
4 B. Kaufman, T. Rozgonyi, P. Marquetand and T. Weinacht, *Phys. Rev. Lett.*, 2020, **125**, 053202.
5 Y. Kobayashi, K. F. Chang, S. M. Poullain, V. Scutelnic, T. Zeng, D. M. Neumark and S. R. Leone, *Phys. Rev. A*, 2020, **101**, 063414.
6 F. Remacle and R. D. Levine, *Proc. Natl. Acad. Sci. U. S. A.*, 2006, **103**, 6793–6798.
7 F. Remacle, M. Nest and R. D. Levine, *Phys. Rev. Lett.*, 2007, **99**, 183902.
8 B. H. Muskatel, F. Remacle and R. D. Levine, *J. Phys. Chem. A*, 2012, **116**, 11311–11318.
9 A. Valentini, S. van den Wildenberg and F. Remacle, *Phys. Chem. Chem. Phys.*, 2020, **22**, 22302–22313.
10 S. Baker, J. S. Robinson, C. A. Haworth, H. Teng, R. A. Smith, C. C. Chirilă, M. Lein, J. W. G. Tisch and J. P. Marangos, *Science*, 2006, **312**, 424.
11 J. P. Marangos, S. Baker, N. Kajumba, J. S. Robinson, J. W. G. Tisch and R. Torres, *Phys. Chem. Chem. Phys.*, 2008, **10**, 35–48.
12 M. Lein, *Phys. Rev. Lett.*, 2005, **94**, 053004.
13 R. F. Frey and E. R. Davidson, *J. Chem. Phys.*, 1988, **88**, 1775–1785.
14 T. Mondal and A. J. C. Varandas, *J. Chem. Phys.*, 2015, **143**, 014304.
15 T. Mondal and A. J. C. Varandas, *J. Chem. Theory Comput.*, 2014, **10**, 3606–3616.
16 T. Mondal and A. J. C. Varandas, *J. Chem. Phys.*, 2011, **135**, 174304.
17 S. Patchkovskii, *Phys. Rev. Lett.*, 2009, **102**, 253602.
18 H. Köppel, W. Domcke and L. S. Cederbaum, in *Advances in Chemical Physics*, ed. I. Prigogine and S. A. Rice, Wiley, 1984, vol. 57, pp. 59–246.
19 C. B. Madsen, M. Abu-samha and L. B. Madsen, *Phys. Rev. A*, 2010, **81**, 043413.
20 H.-J. Werner, P. J. Knowles, G. Knizia, F. R. Manby and M. Schütz, *Wiley Interdiscip. Rev.: Comput. Mol. Sci.*, 2012, **2**, 242–253.
21 R. Weinkauf, P. Schanen, A. Metsala, E. W. Schlag, M. Buergle and H. Kessler, *J. Phys. Chem.*, 1996, **100**, 18567–18585.
22 F. Remacle, R. D. Levine, E. W. Schlag and R. Weinkauf, *J. Phys. Chem. A*, 1999, **103**, 10149–10158.
23 L. S. Cederbaum and J. Zobeley, *Chem. Phys. Lett.*, 1999, **307**, 205–210.
24 T. Kuś, B. Mignolet, R. D. Levine and F. Remacle, *J. Phys. Chem. A*, 2013, **117**, 10513–10525.
25 B. Mignolet, R. D. Levine and F. Remacle, *Phys. Rev. A*, 2012, **86**, 053429.
26 F. Calegari, D. Ayuso, A. Trabattoni, L. Belshaw, S. De Camillis, S. Anumula, F. Frassetto, L. Poletto, A. Palacios, P. Decleva, J. B. Greenwood, F. Martín and M. Nisoli, *Science*, 2014, **346**, 336–339.
27 M. Ben-Nun and R. D. Levine, *J. Chem. Phys.*, 1995, **201**, 163–187.
28 S. A. Jayantha, K. G. Komarova, S. V. D. Wildenberg, F. Remacle and R. D. Levine, in *Attosecond Molecular Dynamics*, ed. M. J. J. Vrakking and F. Lepine, Royal Society of Chemistry, Cambridge, 2018, vol. 13, pp. 308–347.
29 J. S. Ajay, K. G. Komarova, F. Remacle and R. D. Levine, *Proc. Natl. Acad. Sci. U. S. A.*, 2018, **115**, 5890–5895.
30 K. G. Komarova, F. Remacle and R. D. Levine, *J. Chem. Phys.*, 2019, **151**, 114308.
31 K. Komarova, S. vandenWildenberg, F. Remacle and R. D. Levine, *J. Phys. B: At., Mol. Opt. Phys.*, 2020, **53**, 134001.
32 J. Li, J. Lu, A. Chew, S. Han, J. Li, Y. Wu, H. Wang, S. Ghimire and Z. Chang, *Nat. Commun.*, 2020, **11**, 2748.
33 D. Austin, A. Johnson, F. McGrath, D. Wood, L. Miseikis, T. Siegel, P. Hawkins, A. Harvey, Z. Maín, S. Patchkovskii, M. Vacher, J. P. Malhado, M. Ivanov, O. Smirnova and J. Marangos, *Sci. Rep.*, 2021, **11**, 2485.
34 A. H. Winney, G. Basnayake, D. A. Debrah, Y. F. Lin, S. K. Lee, P. Hoerner, Q. Liao, H. B. Schlegel and W. Li, *J. Phys. Chem. Lett.*, 2018, **9**, 2539–2545.
35 R. Geneaux, H. J. B. Marroux, A. Guggenmos, D. M. Neumark and S. R. Leone, *Philos. Trans. R. Soc., A*, 2019, **377**, 20170463.
36 H. Timmers, X. Zhu, Z. Li, Y. Kobayashi, M. Sabbar, M. Hollstein, M. Reduzzi, T. J. Martínez, D. M. Neumark and S. R. Leone, *Nat. Commun.*, 2019, **10**, 3133.
37 K. S. Zinchenko, F. Ardana-Lamas, I. Seidu, S. P. Neville, J. van der Veen, V. U. Lanfaloni, M. S. Schuurman and H. J. Wörner, *Science*, 2021, **371**, 489.
38 D. T. Matselyukh, V. Despré, N. V. Golubev, V. Svoboda, A. I. Kuleff and H. J. Wörner, *The 22nd International Conference on Ultrafast Phenomena 2020*, Washington, D.C., 2020.